Journal of Materials Chemistry A

ROYAL SOCIETY OF CHEMISTRY

PAPER

View Article Online
View Journal

Cite this: DOI: 10.1039/d6ta00171h

Formation and activity mechanisms of a carbon-nitride-supported single-atom catalyst for photocatalytic hydrogen evolution

Yuki Tomoyasu,†[a] Makito Takagi, †[b] Tokuhisa Kawawaki, †*[ac] Md. Mohibul Islam,[a] Yuki Yamazaki,[c] Yamato Shingyouchi,[c] Tomomi Shimazaki, [b] Masanori Tachikawa *[b] and Yuichi Negishi *[ac]

Single-atom catalysts (SACs), which feature isolated single atoms (SAs) of a metal adsorbed on a support, have garnered significant attention as catalysts for a wide range of reactions due to the complete utilization of their active metal sites. However, the fundamental mechanisms governing their formation and exceptional catalytic activity remain largely unelucidated. A major challenge in SAC preparation lies in controlling residual SA precursors and mitigating the aggregation of SAs, particularly at high metal loadings. A comprehensive understanding of these mechanisms is therefore paramount for developing rational design principles to overcome these limitations. In this study, we combined *in situ* X-ray absorption fine structure analysis with density functional theory calculations to elucidate these critical mechanisms. Our findings reveal that (i) the key factors in successful SAC formation are the destabilization of the SA precursor and the suppression of neutral-metal-atom formation; and (ii) the high catalytic activity of SACs is primarily attributed to their maximized number of surface-active sites and that SAs exhibit an optimal hydrogen adsorption energy. These insights provide valuable design guidelines for the future development of diverse and highly active SACs.

Received 7th January 2026
Accepted 21st April 2026

DOI: 10.1039/d6ta00171h

rsc.li/materials-a

Introduction

In recent years, single-atom catalysts (SACs), which feature isolated single atoms (SAs) of a metal dispersed on a support, have attracted significant attention due to their exceptional activity across a wide range of catalytic reactions.[1–6] With advancements in characterization techniques since 2011, research on SACs has accelerated rapidly, and numerous studies have reported their high activity as photo- and electrocatalysts.[4,7] For example, in water-splitting photocatalysts (Fig. 1a),[8–12] which are a key focus for next-generation green hydrogen (H_2) production, various SACs loaded on photocatalysts have demonstrated high efficiency as cocatalysts for the H_2 evolution reaction (HER).[13–29] The primary advantage of SACs over traditional metal-nanoparticles (NPs) catalysts is the complete utilization of their active metal sites. Conventional metal NPs suffer from the fact that their internal atoms do not act in the catalytic reaction. Because SAs have no inert internal atoms, they show dramatically improved reaction efficiency per metal atom.

Nevertheless, the fundamental mechanisms governing SAC formation and their high activity remain largely unknown. SAs are highly reactive and unstable, existing almost exclusively in support-stabilized forms.[3,4] A major challenge in SAC synthesis is controlling residual SA precursors and mitigating aggregation of SAs, particularly at high metal loadings or on supports with low specific surface areas. A comprehensive understanding of these formation mechanisms is crucial for developing precise control strategies to overcome these limitations.

When metal particles decrease a size of approximately 2 nm or smaller, they exhibit quantum size effects, which alter their electronic states from those of typical metal NPs.[30–38] Consequently, SAs possess significantly different physicochemical properties compared with their corresponding bulk metals and metal NPs. This means that the relationship between kind of metal element and catalytic activity can vary drastically between SAs and NPs. Additionally, SAC activity is not solely dependent on the type of SA but also heavily influenced by the structure and composition of the support material. Accordingly, theoretical calculations are essential for predicting catalytic reaction mechanisms.

In this study, we investigated the formation mechanism of SAs on a graphitic-carbon nitride photocatalyst (g-C_3N_4; gCN)

[a]*Institute of Multidisciplinary Research for Advanced Materials, Tohoku University, Katahira 2-1-1, Aoba-ku, Sendai 980-8577, Japan. E-mail: tokuhisa.kawawaki.d8@tohoku.ac.jp; yuichi.negishi.a8@tohoku.ac.jp*

[b]*Quantum Chemistry Division, Yokohama City University, 22-2 Seto, Kanazawa-ku, Yokohama 236-0027, Japan. E-mail: tachi@yokohama-cu.ac.jp*

[c]*Carbon Value Research Center, Research Institute for Science and Technology, Tokyo University of Science, Kagurazaka, Shinjuku-ku, Tokyo 162-8601, Japan*

† These authors contributed equally to this work.

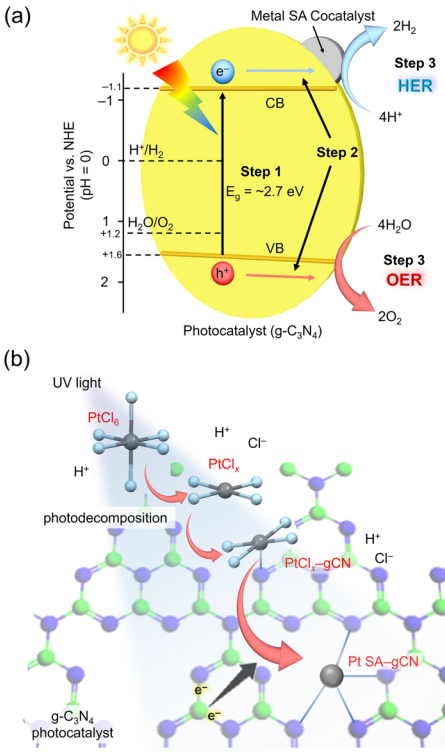

Fig. 1 Schematic of the work performed in this study. (a) Photocatalytic water-splitting using SA cocatalysts on g-C_3N_4, and (b) a proposed mechanism for the formation of SAs on g-C_3N_4 photocatalysts.

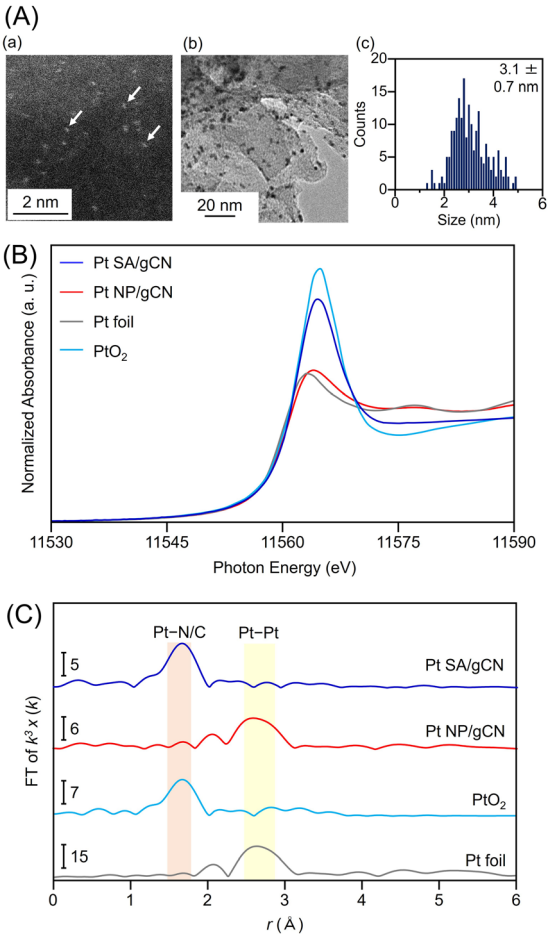

Fig. 2 Characterization of Pt SA/gCN and Pt NP/gCN. (A) TEM and STEM images of (a) PtSA/gCN and (b) Pt NP/gCN and (c) resulting size histogram of Pt particle of Pt NP/gCN. Pt L_3-edge (B) XANES and (C) FT-EXAFS spectra of Pt SA/gCN and Pt NP/gCN. In (B) and (C), Pt L_3-edge XANES and FT-EXAFS spectra of Pt foil and PtO_2 powder are also shown for comparison. In (C), the peaks at ~1.6 and 2.5–2.8 Å are assigned to Pt–C/N and Pt–Pt bonds, respectively. The Pt loading weights were 2.0 and 3.0 wt% for Pt SA/gCN and Pt NP/gCN, respectively.

support by combining *in situ* X-ray absorption fine structure (XAFS) analysis with density functional theory (DFT) calculations (Fig. 1b). We also aimed to explore the catalytic mechanism by which SA-loaded gCN (M SA/gCN) exhibits high activity for photocatalytic water splitting to produce H_2. Our findings revealed that the key factors for successful SAC formation are primarily the destabilization of the SA precursor and the suppression of neutral-metal-atom formation. We also determined that the high activity of M SA/gCN is a result of both an abundance of surface active sites and optimal H_2 adsorption energy of SAs.

Results and discussion

Photocatalytic HER activities of SACs

We prepared SACs based on a previously reported method.[1] We utilized gCN(Fig. S1), a widely studied visible-light-responsive photocatalyst capable of water splitting, as the support. Various metal SAs, specifically Pt, Pd, and Rh, which are known for their high HER activity, were loaded onto the gCN as cocatalysts using a light-induced adsorption method with controlled reducing power (Fig. 2 and S2–S5). For comparison study, a conventional catalyst with 3 wt% Pt NPs (Pt NP/gCN) was prepared following a previously established protocol (Fig. 2 and S6).[11,39]

The photocatalytic activities of the resulting Pt SAC (Pt SA/gCN) and Pt NP/gCN for water splitting are presented in Fig. 3. The Pt SA/gCN catalyst, with an optimized Pt content of 2 wt%, exhibits the highest HER activity.[1] Our results demonstrate that Pt SA/gCN shows a 1.43-fold higher HER activity than that of Pt NP/gCN (Fig. 3a). Furthermore, such high photocatalytic HER activity was observed for at least 12 hours (Fig. S7). Given the high cost of Pt cocatalysts, the HER activity per unit weight of Pt is a critical metric. We therefore calculated this value and found that Pt SA/gCN exhibits 2.13-times more HER activity per Pt loading than that of Pt NP/gCN (Fig. 3b). These findings confirm the superior HER activity of the Pt SA cocatalyst compared with the conventional Pt NP cocatalyst.

To investigate the changes in the state of the Pt SAs during the reaction, we performed XAFS measurements on the pristine Pt SA/gCN and on a sample after photocatalytic activity evaluation (Pt SA/gCN_light), as shown in Fig. S8. The white line peak intensity near 11 565 eV in the Pt L_3-edge X-ray absorption near-edge structure (XANES) spectrum indicates that the as-prepared

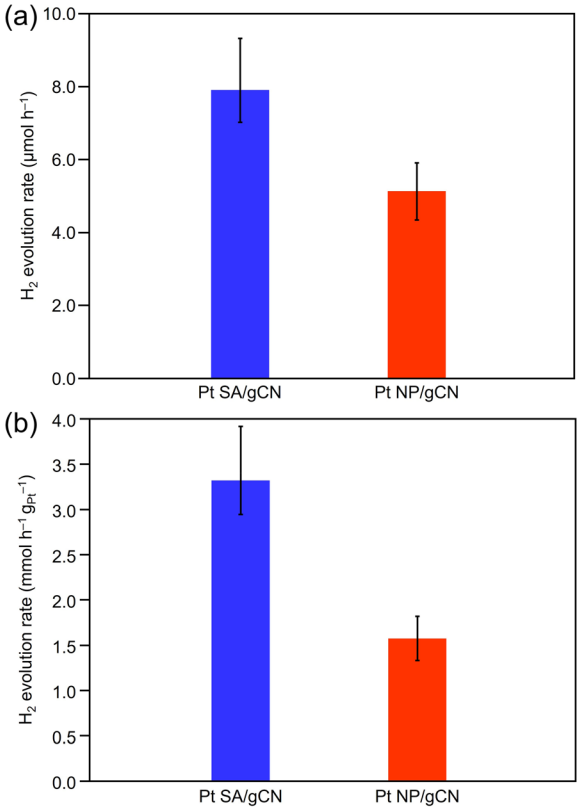

Fig. 3 Photocatalytic hydrogen evolution activities of Pt SA/gCN and Pt NP/gCN under visible-light irradiation (Xe lamp: ≥410 nm). (a) Hydrogen-evolution rate and (b) hydrogen-evolution rate per metal atom for Pt SA/gCN and Pt NP/gCN. In (a) and (b), the Pt loading weights were 2.0 and 3.0 wt% for Pt SA/gCN and Pt NP/gCN, respectively.

Pt SA/gCN has an electronic state approximating Pt(III) or Pt(IV) (Fig. S8(a)). The coexistence of Pt(IV–II) was also confirmed by the results of Pt 4*f* X-ray photoelectron spectroscopy (Fig. S9). Conversely, after 5 h of photoirradiation in the catalytic reaction, the Pt SA/gCN_light sample showed a more reduced electronic state, shifting closer to Pt(II). Furthermore, this reduced Pt(II) state highly stable for extended periods even after light irradiation stopped. While such a reductive change in electronic state is often attributed to the aggregation of SAs into Pt NPs (*i.e.*, the formation of Pt(0)), the results of Fourier transform-extended X-ray absorption fine structure (FT-EXAFS) analysis of the Pt L_3-edge reveal Pt–C/N bonds (~1.6 Å) in both samples, but no Pt–Pt bonds (2.5–2.8 Å) are observed (Fig. S8(b)). A slight decreasing in the strength of the Pt–C/N bonds is observed after photoirradiation. These findings suggest that the photoirradiation-induced electronic state change in Pt SA/gCN is a result of local structural changes rather than the aggregation of Pt SAs. Curve-fitting analysis of the L_3-edge FT-EXAFS spectrum further supports this, showing no Pt–Pt bonds in either sample and a slight decrease in the coordination number and bond length of the Pt–C/N bond after photoirradiation (Table S1). These specific changes in the electronic and bonding states were not observed in Pt NP/gCN, indicating that this is a phenomenon specific to the SAC.

In situ preparation and photocatalytic measurement of SACs

To investigate the photosensitive state changes of the SAs, we performed *in situ* XAFS measurements under photoirradiation. This approach was employed to provide a deeper understanding of the formation mechanism of Pt SAs and the local structural evolution during the photocatalytic reaction.

We used a photoirradiation-capable reaction tube to irradiate gCN with UV light ($\lambda = 365$ nm) in the presence of H_2PtCl_6 as the precursor of SAs (Fig. 4A). The obtained Pt L_3-edge XANES and FT-EXAFS spectra reveal a gradual shift in the Pt electronic state towards the negative side with photoirradiation. This indicates that the Pt(IV) derived from the precursor H_2PtCl_6 evolves into an electronic state closer to Pt(III) over time (Fig. 4A(a and c)). Concurrently, the FT-EXAFS spectra show that the Pt–Cl bond (~2.0 Å) gradually decreases, and a new Pt–C/N bond (~1.6 Å) forms (Fig. 4A(b and c)). This suggests that Pt SAs are formed by the dissociation of the Pt–Cl bond in H_2PtCl_6 and the subsequent formation of a Pt–C/N bond with the gCN support.

Next, we monitored the local structural changes of the Pt SAs during the photocatalytic reaction. We performed *in situ* Pt L_3-edge XAFS measurements on Pt SA/gCN while irradiating it with visible light ($\lambda = 405$ nm) in water with a sacrificial agent (Fig. 4B). The XANES spectrum reveals that the electronic state of the Pt SAs gradually shifts to the negative side, stabilizing at a state close to Pt(II) (Fig. 4B(a and c)). When the light is turned off, this charge state remains unchanged. The FT-EXAFS spectrum shows that the strength of the Pt–C/N bond gradually decreases, and the bond distance shortens with light irradiation (Fig. 4B(b and c)). However, some spectra were noisy due to the generation of H_2 bubbles, which interfere with the spectral analysis.

To confirm the roles of water and the sacrificial agent, we conducted comparative experiments and found that these local electronic and geometric structural changes do not occur in the absence of either component (Fig. S10 and S11). Similarly, other metal SAs (M = Pd, Rh) exhibit a similar pattern: a negative shift in the electronic structure and a decrease in the strength and bond distance of the M–C/N bond (Fig. S12 and S13). Importantly, these changes are not observed with the Pt NP/gCN catalyst, confirming that this phenomenon is unique to the SA state (Fig. S14).

DFT analysis of SACs

To obtain a clearer mechanistic understanding of the experimentally observed results for SAC formation and their high activity, we conducted a deeper analysis using DFT calculations.[40]

We compared the Bader charges of the metal atoms in a series of predicted intermediates for the preparation of SACs. We performed geometry optimization on a number of key reaction intermediates, specifically $PtCl_n$ ($n = 0$–3) adsorbed on gCN, which we represented as $[PtCl_n/gCN]^z$ ($n = 1$–3) and $[Pt\ SA/gCN]^z$. These intermediates were modeled with various charge states (z) ranging from −2 to +2 (Fig. 5A).

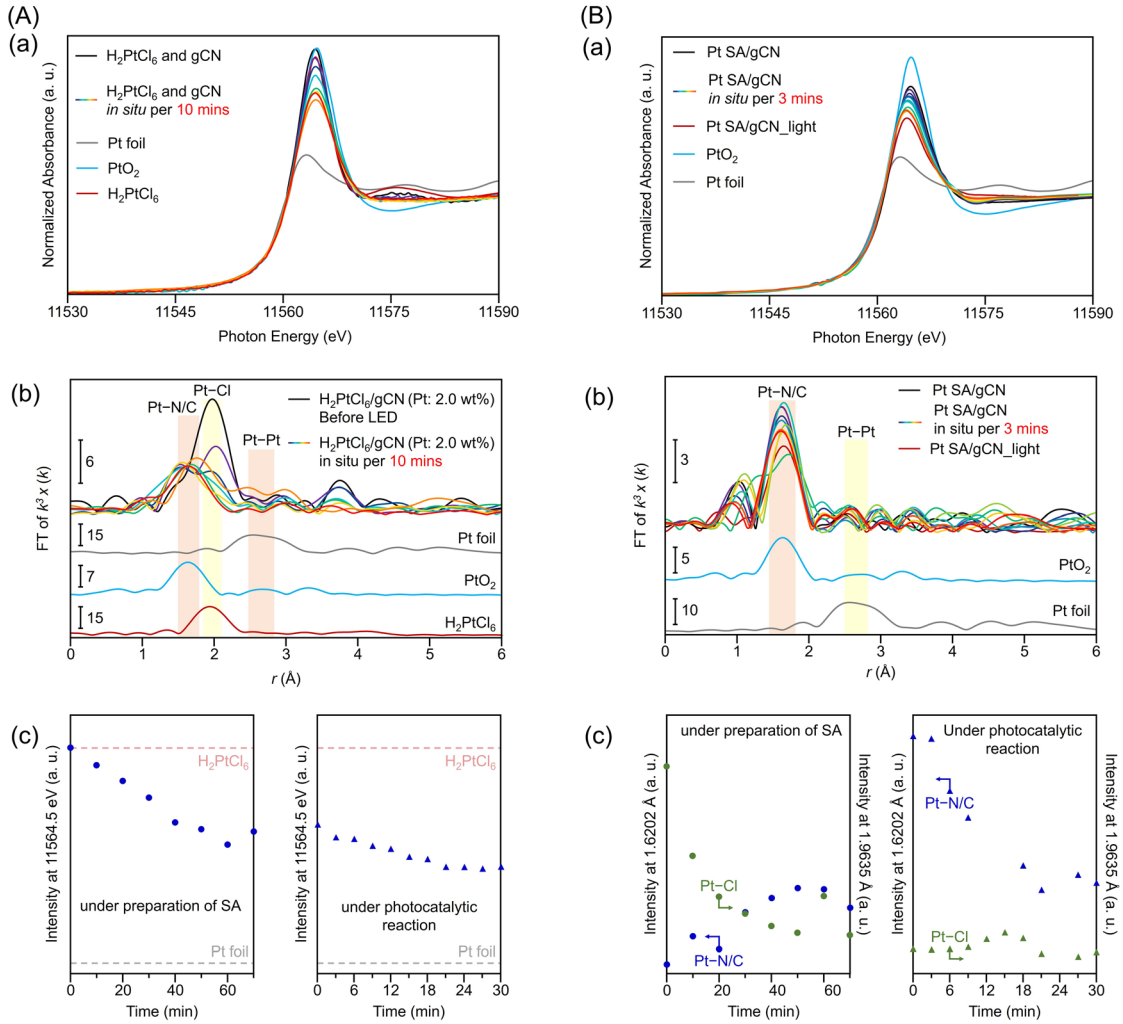

Fig. 4 Results of *in situ* XAFS measurements during light irradiation. Pt L_3-edge (a) XANES and (b) FT-EXAFS spectra of Pt SA/gCN during (A) preparation of SA (light source: 365 nm LED) and (B) photocatalytic reaction (light source: 405 nm LED). (c) Resulting peak-intensity histograms for Pt L_3-edge (a) XANES and (b) FT-EXAFS spectra during preparation of the SAC (light source: 365 nm LED) and photocatalytic reaction (light source: 405 nm LED). In (a) and (b), the Pt L_3-edge XANES and FT-EXAFS spectra of H_2PtCl_6, Pt foil and PtO_2 powder are also shown for comparison. In (b), the peaks at ~1.6, ~2.0, and 2.5–2.8 Å are assigned to Pt–C/N, Pt–Cl, and Pt–Pt bonds, respectively.

First, we analyzed the Bader charges of each Pt atom (Z_{Pt}) in the $[PtCl_n/gCN]^z$ (n = 1–3) and $[Pt\ SA/gCN]^z$ in a vacuum (Fig. 5B(a)). Our results show a clear trend: across almost all samples, as the overall charge (Z_{tot}) becomes more negative, the Z_{Pt} also shifts to a more negative value.

Next, we focused on the intermediates with a neutral overall charge ($[PtCl_n/gCN]^0$ (n = 1–3) and $[Pt\ SA/gCN]^0$). The Z_{Pt} for $[PtCl_3/gCN]^0$ is 0.82, and as the number of chlorine ligands decreases, the Z_{Pt} value becomes progressively more negative, reaching its lowest value of 0.40 for $[Pt\ SA/gCN]^0$. For comparison, the SA precursor, $[H_2PtCl_6]^0$, has a Z_{Pt} of 0.87, the most positive value among all the presumed intermediates. This trend, where the desorption of Cl from the Pt complex shifts Z_{Pt} to a more negative state, is also observed for intermediates with different overall charges. The effect of charge state on Z_{Pt} is even more pronounced when, instead of the model in a vacuum, water is modeled as a solvent (Fig. 5B(b)). Furthermore, overall, the removal of Cl in $[PtCl_n/gCN]^z$ induced the shortening of Pt–N bonds (Table S2–S4). This same behavior is also observed for Ru SA/gCN, suggesting a similar formation mechanism (Fig. S15, Table S5 and S6).

To further elucidate the origins of the high activity observed for SACs, we performed a detailed analysis using DFT calculations (Fig. 5C). We compared the H adsorption energies for the Pt(111) surface, a common crystal facet of Pt NPs, and for Pt SA/gCN in a vacuum. As shown in Fig. 5C(a), H adsorbs on the Pt(111) surface in either an on-top (-64.8 kJ mol^{-1}) or a bridge (-45.9 kJ mol^{-1}) configuration. In contrast, the H adsorption energy for Pt SA/gCN is significantly lower (-92.1 kJ mol^{-1}). The strong adsorption of hydrogen consequently may hinder the final release and formation of hydrogen molecules from the SA site. From a thermodynamic standpoint, this suggests that the HER is more likely to proceed on Pt NPs with a Pt(111) surface rather than on Pt SA/gCN.

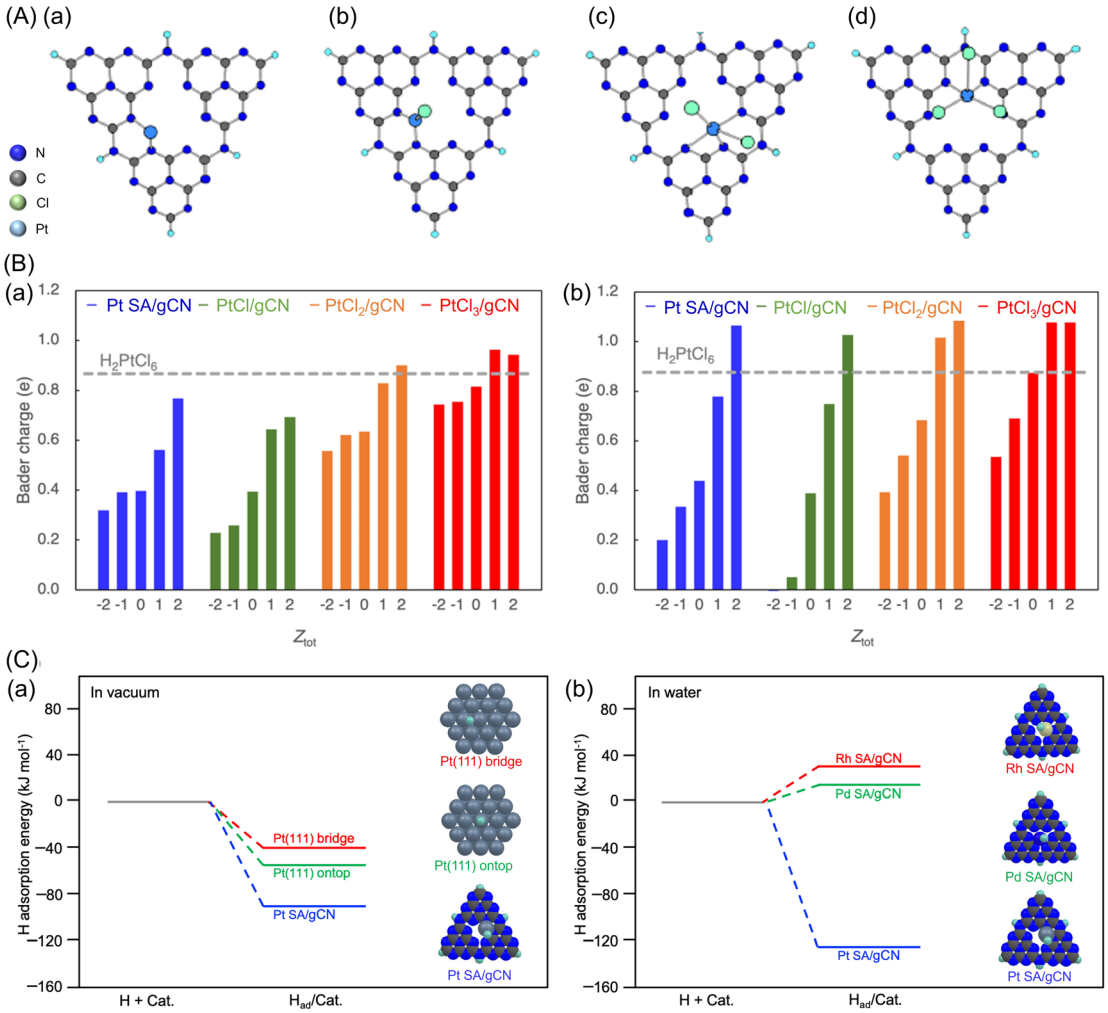

Fig. 5 Results of DFT calculations. (A) The simulation models of (a) Pt SA/gCN, (b) PtCl/gCN, (c) $PtCl_2$/gCN and (d) $PtCl_3$/gCN. (B) Results of Barder charge analysis for Pt (Z_{Pt}) on Pt SA/gCN, $PtCl_n$/gCN, and $PtCl_6$ at each total charge (Z_{tot} from −2 to +2) under (a) vacuum and (b) water. (C) Adsorption energy of a hydrogen atom: (a) on the on-top or bridge sites of Pt(111) and Pt SA/gCN under vacuum, and (b) on M SA/gCN (M = Pt, Pd, Rh) under aqueous conditions. The reference energy is defined as the sum of half of the formation energy of an H_2 molecule and the energy of the non-interacting surface system (*i.e.*, the infinitely separated state).

Our previous work demonstrated that Pd SAs exhibit superior photocatalytic HER activity compared with other metal SACs, such as Pt and Rh.[1] We therefore used DFT calculations to investigate the origin of this metal-species-dependent activity. By comparing the H adsorption energies for various M SA/gCN catalysts (where M = Pt, Pd, or Rh), we found that Pd SA/gCN has the lowest H adsorption energy (Fig. 5C(b), S16 and Table S7 and S8). Conversely, Pt SA/gCN exhibits a lower HER activity owing to its stronger H adsorption energy. This strong correlation between calculated H adsorption energies and our previously reported experimental HER activities supports our hypothesis that the optimal H adsorption energy for HER shifts with a change in metal size. This shift allows Pd SA to function as a highly active cocatalyst for the HER.

SAC-formation mechanism

Based on *in situ* XAFS and DFT calculations, we propose a mechanism for Pt SAC formation, as summarized in Fig. 6A. The Pt SA precursor, H_2PtCl_6, exists as a relatively stable $[PtCl_6]^{2-}$ ion in water (Fig. 6A(a)). This octahedral d^6 species is coordinatively saturated and electronically stable, resulting in negligible interaction with the gCN surface. However, under UV irradiation, the electronic state of $[PtCl_6]^{2-}$ is destabilized through a ligand-to-metal charge transfer (LMCT) transition, initiating a sequence of decomposition and reduction steps.[41–43] As illustrated in our proposed mechanism (Fig. 6A(a)), the photo-excitation generates highly reactive, unstable intermediates—collectively denoted as $PtCl_x$—including $[PtCl_5]^{2-}$, $[PtCl_4(OH)(H_2O)]^{2-}$, $[PtCl_3(OH)]^{-}$, $[PtCl_5(OH)]^{2-}$, $[PtCl_5(H_2O)]^{-}$, $[PtCl_4(OH)(H_2O)]^{-}$, $[PtCl_2(OH)(H_2O)]^{-}$.[42] The nitrogen atoms within the gCN framework, acting as Lewis bases with lone pairs, effectively attack these transient Pt intermediates, forming robust Pt–N coordination bonds that anchor the Pt at the atomic level (Fig. 5A and B).

The UV-vis spectral evolution of H_2PtCl_6 (Fig. 7a) further elucidates the reaction pathway under light irradiation in water.

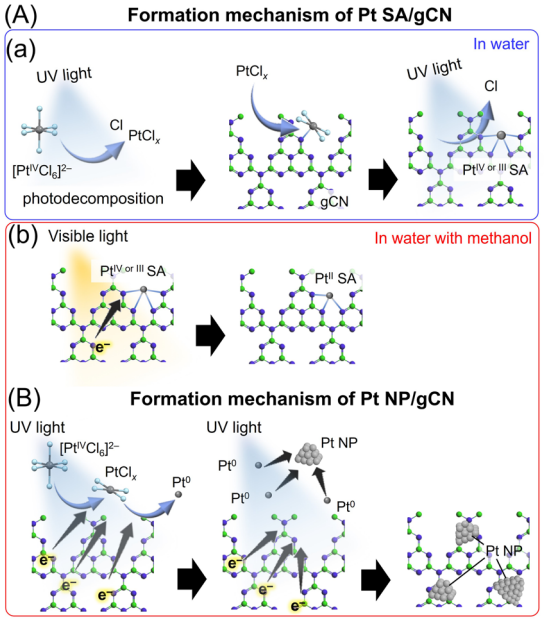

Fig. 6 Schematic showing the proposed mechanism. (A) Proposed (a) formation mechanism during preparation of SA/gCN; (b) local structural changes for SA/gCN during photocatalytic reaction; and (B) proposed formation mechanism for Pt NP/gCN.

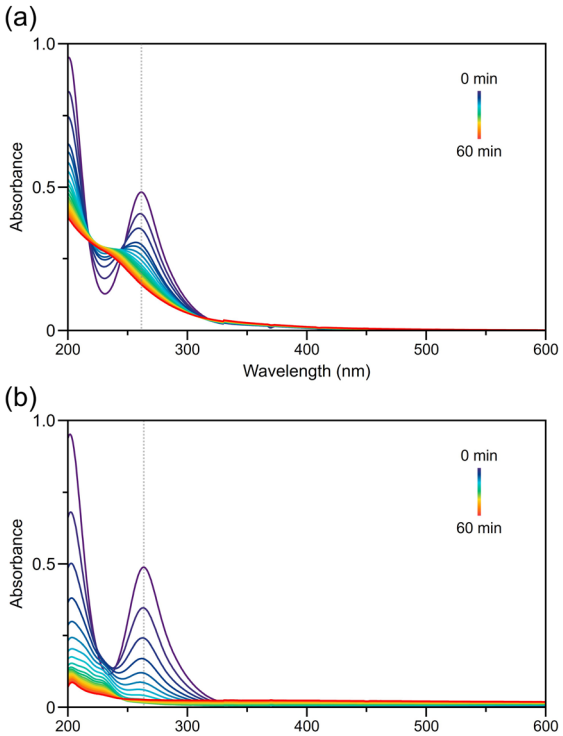

Fig. 7 Tracking results of the photoreductive decomposition reaction of H_2PtCl_6. Time-dependent UV-vis spectra under light irradiation (λ = 405 nm) of 0.02 mM H_2PtCl_6 aqueous solutions (a) without and (b) with methanol (50 vol%).

The decrease in the $[PtCl_6]^{2-}$ peak (~260 nm) and the concomitant emergence of the $[PtCl_4]^{2-}$ peak (~230 nm and 330 nm shoulder) by the ight irradiation confirm the reduction from Pt(IV) to Pt(II). Notably, this transformation proceeds even in the absence of gCN, indicating a self-reducing chain reaction involving the disproportionation of Pt(III) intermediates (2 Pt(III) to Pt(IV) + Pt(II)). Crucially, our control experiment revealed that adding gCN to $[PtCl_4]^{2-}$ solution does not result in SAC formation. This indicates that the stable Pt(II) end-product is not the active species for immobilization. Instead, the trapping of Pt onto the support must occur during the transient window when unstable $PtCl_x$ intermediates are present.

In these coordinatively unsaturated intermediates ($PtCl_x$), at least one coordination site is either vacant or occupied by a labile water molecule. The exceptionally low activation energy (E_a) of 3.67 kJ mol^{-1} obtained from the Arrhenius plot (Fig. S17), derived from Fig. 7a, provides strong evidence for this non-thermal pathway. This value is nearly an order of magnitude lower than the typical thermal barriers for ligand exchange reactions (tens of kJ mol^{-1}), which involve the vibrationally-excited cleavage of metal–ligand bonds. Consistent with the mechanistic framework proposed by Glebov *et al.*,[42] we attribute the remarkably low E_a to the formation of a geminate radical pair. Upon photo-excitation, the $[PtCl_6]^{2-}$ complex undergoes homolytic scission to form a $\{[PtCl_5]^{2-}\cdot Cl^{\bullet}\}$ pair confined within a solvent cage as is well-established in the Frank–Rabinowitch model. Because the substantial energy required for this primary bond cleavage is provided by incident photons rather than thermal energy, it is effectively decoupled from the observed activation barrier. Consequently, the measured unusually low E_a likely reflects the minimal physical barrier associated with "cage escape"—the diffusion of the radical species out of the solvent cage— or the low-barrier propagation steps of the Pt(III)-mediated chain reaction.

Finally, once the $PtCl_x$ are anchored on gCN, subsequent photoreductive halogen desorption gradually removes the remaining Cl ligands (Fig. 4C(b));[41–46] thereafter, these atoms are further stabilized in a Pt(II) state through electron transfer from the photo-excited gCN, ultimately yielding a stable and atomically dispersed Pt catalyst (Fig. 6A(b)).

Interestingly, the presence of methanol as a sacrificial agent during light irradiation leads to the formation of Pt NPs instead of SAs on gCN (Fig. 6B). The formation of Pt NPs is generally understood to occur in three distinct steps:[32,47] (i) the reduction of precursor Pt complexes to form Pt(0) atoms; (ii) the nucleation of Pt nanoclusters (NCs) *via* the aggregation of these Pt(0) atoms; and (iii) the subsequent growth of these NCs. The role of the sacrificial agent is thought to suppress of charge recombination in the photocatalyst, and scavenge Cl$^{\bullet}$ radicals, thereby facilitating multi-electron reduction. Furthermore, the addition of alcohol also promotes photoinduced dissociation of $[PtCl_6]^{2-}$ to Pt(0) in water even in the absence of a photocatalyst.[41,47] This was also confirmed by the fact that when light is irradiated onto $[PtCl_6]^{2-}$ in an aqueous solution containing methanol, absorption in the visible region (>400 nm) increases due to the formation of Pt NCs (Fig. 7b and S18). This efficient reduction promotes the rapid and efficient progression of step (i), leading to a high concentration of Pt(0) atoms in the aqueous solution. The presence of high concentrations of Pt(0) atoms is expected

to promote steps (ii) and (iii), leading to the formation of Pt NPs. However, without the sacrificial agent, the reduction is less efficient, and the unstable intermediate species formed are thought to adsorb onto the gCN support before a multi-electron reduction to Pt(0) can occur. This adsorption is what leads to the formation of SAs. Once the SAs are formed and stabilized on the gCN, their relatively high structural stability prevents their aggregation into NPs.

Highly active mechanism of SACs

As shown in Fig. 3, Pt SA/gCN exhibits superior photocatalytic HER activity compared to Pt NP/gCN. To elucidate the origin of this enhancement, we examined the impact of SA introduction on the light absorption property and conductivity of gCN. Our results indicate no significant alterations in these properties upon Pt SA loading (Fig. S2(d) and S19). Our DFT calculations suggested that the Pt(111) surface is more favorable for the HER than Pt SA/gCN based on H adsorption energy. To validate this, we compared values for the activity per surface Pt atom. Using the average particle size (3.1 ± 0.7 nm) from transmission electron microscopy (TEM) images of Pt NP/gCN (Fig. 2A(b)), we calculated the number of surface Pt atoms, assuming a face-centered cubic (fcc) model (Table S9). The surface Pt atoms account for approximately 36% of the total Pt atoms in Pt NP/gCN. When we calculated the HER activity per surface Pt atom, we found that Pt NP/gCN exhibits 1.28-times the HER activity of Pt SA/gCN. This finding is consistent with our DFT calculations, which indicate that the surface Pt atoms in Pt NP/gCN are inherently more favorable for HER than those in Pt SA/gCN. We attribute the superior HER activity of Pt SA/gCN primarily to its significantly higher atomic utilization. Specifically, while the activity per Pt atom is lower for Pt SA than for Pt NP, the absence of internal atoms in Pt SA ensures that 100% of the Pt atoms are available for the reaction, compared to only 36% for Pt NP/gCN (Table S9). This high density of accessible active sites enables the overall photocatalytic HER activity of Pt SA/gCN to surpass that of Pt NP/gCN (Fig. 3).

However, our previous research showed that M SA/gCN (M = Pd or Rh) exhibits higher HER activity per atom than both Pt SA/gCN and Pt NP/gCN.[1] This observation cannot be explained solely by the increased surface-metal atomic ratio. While Pt NPs are generally known to have higher HER activity than Pd NPs,[48–51] this relationship is reversed for SACs. We considered that this is because the electronic structure of Pd and Rh SAs changes with decreasing size, making it more suitable for H adsorption.

Our DFT calculation results are in good agreement with our previously reported findings on the metal-species dependence of HER activity.[1] We expect that even more active photocatalysts can be created by combining these two (SA and support materials), as more precise changes in the electronic structure of SAs are possible through support control.[52]

Conclusions

In this study, we combined *in situ* XAFS measurements and DFT calculations to elucidate the fundamental mechanisms governing the performance of SACs as cocatalysts for water splitting photocatalysis. Our key findings are as follows:

Pt SAs exhibit a 2.13-fold higher HER activity per unit weight of Pt compared with Pt NPs. The superior performance of Pt SAs is primarily attributed to a maximized ratio of surface-exposed Pt atoms.

The catalytic activities of different metal SACs vary significantly. Rh and Pd SAs demonstrate higher HER activities than Pt SAs. DFT calculations revealed that Pt SA exhibits an excessively strong H adsorption energy, which is thermodynamically unfavorable for the HER. In contrast, Rh and Pd SAs exhibit more suitable H adsorption energies, leading to their higher catalytic efficiencies.

The critical factors for successful SAC formation were identified as the destabilization of the SA precursor and the suppression of neutral-metal-atom formation.

Without sufficient destabilization of the SA precursor, its conversion to an SA state does not occur. However, excessive reduction of the precursor can lead to the formation of neutral metal atoms, which readily aggregate and form metal NPs.

These results provide crucial insights into the functional mechanisms of SACs, clarifying how they achieve high catalytic activity. The SAC formation mechanism elucidated in this study offers a valuable strategic framework for the future synthesis of a wide range of SACs,[53–60] potentially extending beyond light-driven processes. This approach demonstrates exceptional generalizability to various metal species and supports (Fig. S20–S24).[1]

Experimental

In situ XAFS measurement

In situ XAFS measurements were performed with a LED lamp (Asahi Spectra, CL-1501) with a LED head unit at 365 nm or 405 nm (Asahi Spectra, CL-H1-365-9-1 B, or CL-H1-405-9-1-B). In preparation of Pt SA/gCN, $H_2PtCl_6 \cdot 6H_2O$ (200 μL, 10 mM) and gCN (20 mg) were added to a disposable UV cell (optical path length 10 mm) sealed with a paraffin film. The suspension was irradiated with 365 nm of LED and the Pt L_3-edge XAFS spectra was recorded every 10 minutes in transmission mode under the same conditions as above. In photocatalytic reaction of M SA/gCN (M = Pt, Pd or Rh) or Pt NP/gCN, the photocatalyst and 25 wt% TIPA as a sacrificial reagent were mixed and grinded in an agate mortar. The samples (10 mg) were pelletized and added to a disposable UV cell sealed with a paraffin film. The samples were irradiated with 405 nm of LED and the Pt L_3-edge XAFS spectra were recorded every 3 minutes in transmission mode.

Computational details for M SA/gCN

The structures shown in Fig. 5A of the main text were used as models for density functional theory (DFT) calculations of M SA/gCN. To obtain geometrically optimized structures for M SA and Cl ligands, the gCN structure was fixed during both the geometry optimization and vibrational frequency calculations. For systems with an even number of electrons, both singlet and triplet spin states were considered, and the more stable spin

state is discussed in this study. For systems with an odd number of electrons, the doublet spin state was considered. For the Pt(111) surface calculations, a Pt_{31} cluster model was employed, and all atoms except for the central seven Pt atoms were kept fixing during both the geometry optimizations vibrational frequency calculations. Electronic structure calculations were performed using the generalized gradient approximation (GGA) with the Perdew–Burke–Ernzerhof (PBE) functional,[61] employing the 6-31G* basis set for H, C, N, and Cl, and the LANL2DZ basis set for Ru, Rh, Pd, and Pt. Grimme's D3 dispersion correction was also applied.[62] To account for water solvent effects, we employed the polarizable continuum model (PCM) using the integral equation formalism variant (IEF-PCM).[63] All DFT calculations were carried out using Gaussian 16 Rev. C.02.[64] Bader charge analysis was performed using the Henkelman group's code.[65–67] The molecular model of g-C_3N_4 was constructed based on previous reports.[68,69]

Time-dependent UV-vis spectra

Time-dependent UV-vis spectra of H_2PtCl_6 was monitored using 0.02 mM H_2PtCl_6 aqueous solution, with (10−50 vol%) or without methanol. The UV-vis spectrum of the solution was measured after irradiation with a LED lamp (λ = 405 nm) for a fixed period.

Author contributions

T. Kawawaki and Y. Negishi designed the experiments and conducted the measurements with Y. Tomoyasu, M. M. Islam, Y. Yamazaki and Y. Shingyouchi. M. Takagi, T. Shimazaki and M. Tachikawa performed the DFT calculations. T. Kawawaki, M. Tachikawa and Y. Negishi wrote the paper. All authors approved the final version of the manuscript.

Conflicts of interest

There are no conflicts to declare.

Data availability

Relevant data are available from the corresponding authors upon reasonable request.

Supplementary information (SI) is available. See DOI: https://doi.org/10.1039/d6ta00171h.

Acknowledgements

This work was based on results obtained from a project commissioned by the Environment Research and Technology Development Fund (JPMEERF20255RA2) of the Environmental Restoration and Conservation Agency. This work was supported by JST FOREST Program, Grant Number JPMJFR245R. It was also supported by the Japan Society for the Promotion of Science (JSPS) through KAKENHI grants (grant numbers 23H00289, 22K19012, and 24K01459) and "Crossover Alliance to Create the Future with People, Intelligence". Funding from the Carbon Recycling Fund Institute, the Japan Gas Association, the Iwatani Naoji Foundation, the Ichimura Foundation for New Technology, the Suzuki Foundation, the Japan Keirin Autorace Foundation and Tobe-Maki Foundation are gratefully acknowledged.

Notes and references

1 Y. Akinaga, T. Kawawaki, H. Kameko, Y. Yamazaki, K. Yamazaki, Y. Nakayasu, K. Kato, Y. Tanaka, A. T. Hanindriyo, M. Takagi, T. Shimazaki, M. Tachikawa, A. Yamakata and Y. Negishi, *Adv. Funct. Mater.*, 2023, **33**, 2303321.
2 J. N. Tiwari, A. N. Singh, S. Sultan and K. S. Kim, *Adv. Energy Mater.*, 2020, **10**, 2000280.
3 Q. Zhang and J. Guan, *Adv. Funct. Mater.*, 2020, **30**, 2000768.
4 W. Song, C. Xiao, J. Ding, Z. Huang, X. Yang, T. Zhang, D. Mitlin and W. Hu, *Adv. Mater.*, 2024, **36**, 2301477.
5 S. Wang, L. Wang, D. Wang and Y. Li, *Energy Environ. Sci.*, 2023, **16**, 2759–2803.
6 Y. Gao, B. Liu and D. Wang, *Adv. Mater.*, 2023, **35**, 2209654.
7 K. L. Zhou, Z. Wang, C. B. Han, X. Ke, C. Wang, Y. Jin, Q. Zhang, J. Liu, H. Wang and H. Yan, *Nat. Commun.*, 2021, **12**, 3783.
8 Q. Wang and K. Domen, *Chem. Rev.*, 2020, **120**, 919–985.
9 A. Kudo and Y. Miseki, *Chem. Soc. Rev.*, 2009, **38**, 253–278.
10 D. Hirayama, T. Kawawaki, S. Oguchi, M. Ogano, N. Kon, T. Yasuda, A. Higami and Y. Negishi, *J. Am. Chem. Soc.*, 2024, **146**, 26808–26818.
11 D. Yazaki, T. Kawawaki, D. Hirayama, M. Kawachi, K. Kato, S. Oguchi, Y. Yamaguchi, S. Kikkawa, Y. Ueki, S. Hossain, D. J. Osborn, F. Ozaki, S. Tanaka, J. Yoshinobu, G. F. Metha, S. Yamazoe, A. Kudo, A. Yamakata and Y. Negishi, *Small*, 2023, **19**, 2208287.
12 D. Yazaki, T. Kawawaki, T. Tanaka, D. Hirayama, Y. Shingyouchi and Y. Negishi, *Energy Adv.*, 2023, **2**, 1148–1154.
13 J. Yang, X. Zheng, S. S. A. Shah, C. Wang, X. Li, Z. Yan and L. Peng, *Carbon Energy*, 2025, **7**, e695.
14 W. Liu, L. Cao, W. Cheng, Y. Cao, X. Liu, W. Zhang, X. Mou, L. Jin, X. Zheng, W. Che, Q. Liu, T. Yao and S. Wei, *Angew. Chem., Int. Ed.*, 2017, **56**, 9312–9317.
15 Y. Li, Y. Wang, C.-L. Dong, Y.-C. Huang, J. Chen, Z. Zhang, F. Meng, Q. Zhang, Y. Huangfu, D. Zhao, L. Gu and S. Shen, *Chem. Sci.*, 2021, **12**, 3633–3643.
16 X. Jin, R. Wang, L. Zhang, R. Si, M. Shen, M. Wang, J. Tian and J. Shi, *Angew. Chem., Int. Ed.*, 2020, **59**, 6827–6831.
17 X.-H. Jiang, L.-S. Zhang, H.-Y. Liu, D.-S. Wu, F.-Y. Wu, L. Tian, L.-L. Liu, J.-P. Zou, S.-L. Luo and B.-B. Chen, *Angew. Chem., Int. Ed.*, 2020, **59**, 23112–23116.
18 X. Xiao, Y. Gao, L. Zhang, J. Zhang, Q. Zhang, Q. Li, H. Bao, J. Zhou, S. Miao, N. Chen, J. Wang, B. Jiang, C. Tian and H. Fu, *Adv. Mater.*, 2020, **32**, 2003082.
19 L. Zhang, R. Long, Y. Zhang, D. Duan, Y. Xiong, Y. Zhang and Y. Bi, *Angew. Chem., Int. Ed.*, 2020, **59**, 6224–6229.
20 N. Wang, J. Wang, J. Hu, X. Lu, J. Sun, F. Shi, Z.-H. Liu, Z. Lei and R. Jiang, *ACS Appl. Energy Mater.*, 2018, **1**, 2866–2873.

21 P. Zhou, F. Lv, N. Li, Y. Zhang, Z. Mu, Y. Tang, J. Lai, Y. Chao, M. Luo, F. Lin, J. Zhou, D. Su and S. Guo, *Nano Energy*, 2019, **56**, 127–137.
22 P. Zhou, N. Li, Y. Chao, W. Zhang, F. Lv, K. Wang, W. Yang, P. Gao and S. Guo, *Angew. Chem., Int. Ed.*, 2019, **121**, 14322–14326.
23 Y. Sun, J. Lin, W. Yang, X. Chen, H. Zhang, Y. Liu, H. Qi, B. Song, G. Zuo, S. Yang, H. He, F. Yu and Z. Chen, *Small*, 2025, **21**, 2408655.
24 L. Liu, X. Wu, L. Wang, X. Xu, L. Gan, Z. Si, J. Li, Q. Zhang, Y. Liu, Y. Zhao, R. Ran, X. Wu, D. Weng and F. Kang, *Commun. Chem.*, 2019, **2**, 18.
25 Y. Cao, D. Wang, Y. Lin, W. Liu, L. Cao, X. Liu, W. Zhang, X. Mou, S. Fang, X. Shen and T. Yao, *ACS Appl. Energy Mater.*, 2018, **1**, 6082–6088.
26 S. Cao, H. Li, T. Tong, H.-C. Chen, A. Yu, J. Yu and H. M. Chen, *Adv. Funct. Mater.*, 2018, **28**, 1802169.
27 Y. Cao, S. Chen, Q. Luo, H. Yan, Y. Lin, W. Liu, L. Cao, J. Lu, J. Yang, T. Yao and S. Wei, *Angew. Chem., Int. Ed.*, 2017, **56**, 12191–12196.
28 Y. Li, Z. Wang, T. Xia, H. Ju, K. Zhang, R. Long, Q. Xu, C. Wang, L. Song, J. Zhu, J. Jiang and Y. Xiong, *Adv. Mater.*, 2016, **28**, 6959–6965.
29 H. Su, W. Che, F. Tang, W. Cheng, X. Zhao, H. Zhang and Q. Liu, *J. Phys. Chem. C*, 2018, **122**, 21108–21114.
30 T. Kawawaki, Y. Mitomi, N. Nishi, R. Kurosaki, K. Oiwa, T. Tanaka, H. Hirase, S. Miyajima, Y. Niihori, D. J. Osborn, T. Koitaya, G. F. Metha, T. Yokoyama, K. Iida and Y. Negishi, *Nanoscale*, 2023, **15**, 7272–7279.
31 S. Funaki, T. Kawawaki, T. Okada, K. Takemae, S. Hossain, Y. Niihori, T. Naito, M. Takagi, T. Shimazaki, S. Kikkawa, S. Yamazoe, M. Tachikawa and Y. Negishi, *Nanoscale*, 2023, **15**, 5201–5208.
32 T. Kawawaki, N. Shimizu, Y. Mitomi, D. Yazaki, S. Hossain and Y. Negishi, *Bull. Chem. Soc. Jpn.*, 2021, **94**, 2853–2870.
33 T. Kawawaki, T. Okada, K. Takemae, S. Tomihari and Y. Negishi, *ChemNanoMat*, 2024, **10**, e202300575.
34 T. Kawawaki and Y. Negishi, *Dalton Trans.*, 2023, **52**, 15152–15167.
35 R. Jin, C. Zeng, M. Zhou and Y. Chen, *Chem. Rev.*, 2016, **116**, 10346–10413.
36 I. Chakraborty and T. Pradeep, *Chem. Rev.*, 2017, **117**, 8208–8271.
37 Y. Du, H. Sheng, D. Astruc and M. Zhu, *Chem. Rev.*, 2020, **120**, 526–622.
38 K. Takemae, S. Tomihari, T. Naito, M. Takagi, T. Shimazaki, T. Kawawaki, M. Tachikawa and Y. Negishi, *Nanoscale*, 2025, **17**, 3721–3727.
39 G. Zhang, Z.-A. Lan, L. Lin, S. Lin and X. Wang, *Chem. Sci.*, 2016, **7**, 3062–3066.
40 A. Tri Hanindriyo, M. Takagi, Y. Tanaka, T. Kawawaki, Y. Negishi, T. Shimazaki and M. Tachikawa, *Chem. Phys.*, 2025, **588**, 112478.
41 M. Harada and H. Einaga, *Langmuir*, 2006, **22**, 2371–2377.
42 E. M. Glebov and V. F. Plyusnin, *High Energy Chem.*, 2021, **55**, 203–211.
43 I. V. Znakovskaya, Y. A. Sosedova, E. M. Glebov and V. P. Grivin, *Photochem. Photobiol. Sci.*, 2005, **4**, 897–902.
44 K. J. Dwyer, M. Dreyer and R. E. Butera, *J. Phys. Chem. A*, 2019, **123**, 10793–10803.
45 S. G. Newman and M. Lautens, *J. Am. Chem. Soc.*, 2011, **133**, 1778–1780.
46 V. P. Grivin, I. V. Khmelinski, V. F. Plyusnin, I. I. Blinov and K. P. Balashev, *J. Photochem. Photobiol., A*, 1990, **51**, 167–178.
47 S. Chen, Q. Yang, H. Wang, S. Zhang, J. Li, Y. Wang, W. Chu, Q. Ye and L. Song, *Nano Lett.*, 2015, **15**, 5961–5968.
48 Q. Zhu, Z. Xu, B. Qiu, M. Xing and J. Zhang, *Small*, 2021, **17**, 2101070.
49 C. M. Pelicano and H. Tong, *Appl. Res.*, 2024, **3**, e202300080.
50 S. Trasatti, *J. Electroanal. Chem. Interfacial Electrochem.*, 1972, **39**, 163–184.
51 X. Li, X. Hao, A. Abudula and G. Guan, *J. Mater. Chem. A*, 2016, **4**, 11973–12000.
52 L. Gloag, S. V. Somerville, J. J. Gooding and R. D. Tilley, *Nat. Rev. Mater.*, 2024, **9**, 173–189.
53 Y. Shang, X. Xu, B. Gao, S. Wang and X. Duan, *Chem. Soc. Rev.*, 2021, **50**, 5281–5322.
54 Z. Liang, J. Shen, X. Xu, F. Li, J. Liu, B. Yuan, Y. Yu and M. Zhu, *Adv. Mater.*, 2022, **34**, 2200102.
55 J. Lin, W. Tian, Z. Guan, H. Zhang, X. Duan, H. Wang, H. Sun, Y. Fang, Y. Huang and S. Wang, *Adv. Funct. Mater.*, 2022, **32**, 2201743.
56 P. Liu, Y. Zhao, R. Qin, S. Mo, G. Chen, L. Gu, D. M. Chevrier, P. Zhang, Q. Guo, D. Zang, B. Wu, G. Fu and N. Zheng, *Science*, 2016, **352**, 797–800.
57 H. Wei, K. Huang, D. Wang, R. Zhang, B. Ge, J. Ma, B. Wen, S. Zhang, Q. Li, M. Lei, C. Zhang, J. Irawan, L.-M. Liu and H. Wu, *Nat. Commun.*, 2017, **8**, 1490.
58 Q. Wang, Y.-B. Liao, B. Mei, J. Zhang, D. Kido, W. Cheng, G. Chen, T. Zhang, Y. Cao, S.-L. Li, Y. Yan and Y.-Q. Lan, *Angew. Chem., Int. Ed.*, 2025, **64**, e202513656.
59 S. Chen and P. Liu, *Mater. Chem. Front.*, 2024, **8**, 1334–1348.
60 Y. He, Y. Zhang, G. Hao, W. Jiang and J. Di, *Nanoscale*, 2024, **16**, 22077–22098.
61 J. P. Perdew, K. Burke and M. Ernzerhof, *Phys. Rev. Lett.*, 1996, **77**, 3865–3868.
62 S. Grimme, J. Antony, S. Ehrlich and H. Krieg, *J. Chem. Phys.*, 2010, **132**, 154104.
63 A. V. Marenich, C. J. Cramer and D. G. Truhlar, *J. Phys. Chem. B*, 2009, **113**, 6378–6396.
64 M. J. Frisch, G. W. Trucks, H. B. Schlegel, G. E. Scuseria, M. A. Robb, J. R. Cheeseman, G. Scalmani, V. Barone, G. A. Petersson, H. Nakatsuji, X. Li, M. Caricato, A. V. Marenich, J. Bloino, B. G. Janesko, R. Gomperts, B. Mennucci, H. P. Hratchian, J. V. Ortiz, A. F. Izmaylov, J. L. Sonnenberg, D. Williams-Young, F. Ding, F. Lipparini, F. Egidi, J. Goings, B. Peng, A. Petrone, T. Henderson, D. Ranasinghe, V. G. Zakrzewski, J. Gao, N. Rega, G. Zheng, W. Liang, M. Hada, M. Ehara, K. Toyota, R. Fukuda, J. Hasegawa, M. Ishida, T. Nakajima, Y. Honda, O. Kitao, H. Nakai, T. Vreven, K. Throssell, J. A. Montgomery Jr., J. E. Peralta, F. Ogliaro, M. J. Bearpark, J. J. Heyd, E. N. Brothers, K. N. Kudin,

V. N. Staroverov, T. A. Keith, R. Kobayashi, J. Normand, K. Raghavachari, A. P. Rendell, J. C. Burant, S. S. Iyengar, J. Tomasi, M. Cossi, J. M. Millam, M. Klene, C. Adamo, R. Cammi, J. W. Ochterski, R. L. Martin, K. Morokuma, O. Farkas, J. B. Foresman, and D. J. Fox, *Gaussian 16*, Revision C.02, Gaussian, Inc., Wallingford CT, 2016.

65 G. Henkelman, A. Arnaldsson and H. Jónsson, *Comput. Mater. Sci.*, 2006, **36**, 354–360.

66 E. Sanville, S. D. Kenny, R. Smith and G. Henkelman, *J. Comput. Chem.*, 2007, **28**, 899–908.

67 W. Tang, E. Sanville and G. Henkelman, *J. Phys. Condens. Matter*, 2009, **21**, 084204.

68 S. Ye, F. Liu, F. She, J. Chen, D. Zhang, A. Kumatani, H. Shiku, L. Wei and H. Li, *Angew. Chem., Int. Ed.*, 2025, **64**, e202425402.

69 N. Allasia, S. Xu, S. F. Jafri, E. Borfecchia, L. A. Cipriano, G. Terraneo, S. Tosoni, L. Mino, G. Di Liberto, G. Pacchioni and G. Vilé, *Small*, 2025, **21**, 2408286.

